# *Supplementary Materials for*

# "Lower-crustal rupture of the 1952 $M_W$ 6.3 suburban Pyongyang earthquake: insights into seismogenic reactivation in a paleo-collision zone and seismic hazard potential"

Tae-Kyung Hong[1*], Junhyung Lee[1], Byeongwoo Kim[1], Seongjun Park[1], Jeongin Lee[1], Dong Geon Kim[1], and Tae-Seob Kang[2]

## Affiliation and address:

[1]Yonsei University, Department of Earth System Sciences, 50 Yonsei-ro, Seodaemun-gu Seoul 03722, South Korea

[2]Pukyong National University, Division of Earth Environmental System Science, Busan 48513, South Korea

## Correspondence to:

tkhong@yonsei.ac.kr (Tae-Kyung Hong)

# Contents of this file



# Introduction

The supplementary materials provide additional information on the data and results.

# Additional information

We collect seismic waveforms from three long-period analog seismographs (Figs. S1, S2, S3). The theoretical arrival times of major phases are indicated on the waveforms. The analog waveforms are digitized for analysis. The seismic waveforms are corrected for instrument responses (Fig. S4).

The 19 March 1952 $M_W$6.3 suburban Pyongyang earthquake induced stress in the source region. We calculate the Coulomb stress changes for optimally-oriented strike-slip faults and optimally-oriented normal faults at a depth of 10 km for different empirical source-parameter scaling relationships (Blaser et al., 2010; Thingbaijam et al., 2017; Brengman et al., 2019; Liu et al., 2023) to examine possible variations. We find that the observed induced stress fields are similar (Figs. S5 and S6). We assess the Coulomb stress changes for optimally-oriented strike-slip faults and optimally-oriented normal faults at a depth of 30 km based on the scaling relationship of Blaser et al. (2010) (Fig. S7). The earthquake induced negative Coulomb stress changes in the north and south of the epicenter.

We conduct numerical simulation of strong ground motions for hypothetical earthquakes with magnitudes of $M_W$ 5.0-7.0 and focal depths of 10-30 km. The peak ground accelerations (PGAs) and seismic intensities are estimated (Figs. S8, S9, S10, S11). The PGAs and seismic intensities generally increase with increasing magnitude and decreasing focal depth. Current seismicity is concentrated in the region of high PGAs. The PGAs decrease exponentially with distance from the epicenter.

# References

Blaser, L., Krüger, F., Ohrnberger, M., and Scherbaum, F. (2010). Scaling relations of earthquake source parameter estimates with special focus on subduction environment. Bulletin of the Seismological Society of America, 100(6), 2914-2926.

Brengman, C. M., Barnhart, W. D., Mankin, E. H., and Miller, C. N. (2019). Earthquake?scaling relationships from geodetically derived slip distributions. Bulletin of the Seismological Society of America, 111(5), 2696-2719.

Liu, Q. Y., Li, D. Q., Tang, X. S., and Du, W. (2023). New empirical earthquake source?scaling laws. Predictive models for seismic source parameters based on machine learning and general orthogonal regression approaches. Bulletin of the Seismological Society of America, 113(6), 2363-2376.

Thingbaijam, K. K. S., Mai, P. M., and Goda, K. (2017). New empirical earthquake source?scaling laws. Bulletin of the Seismological Society of America, 107(5), 2225-2246.

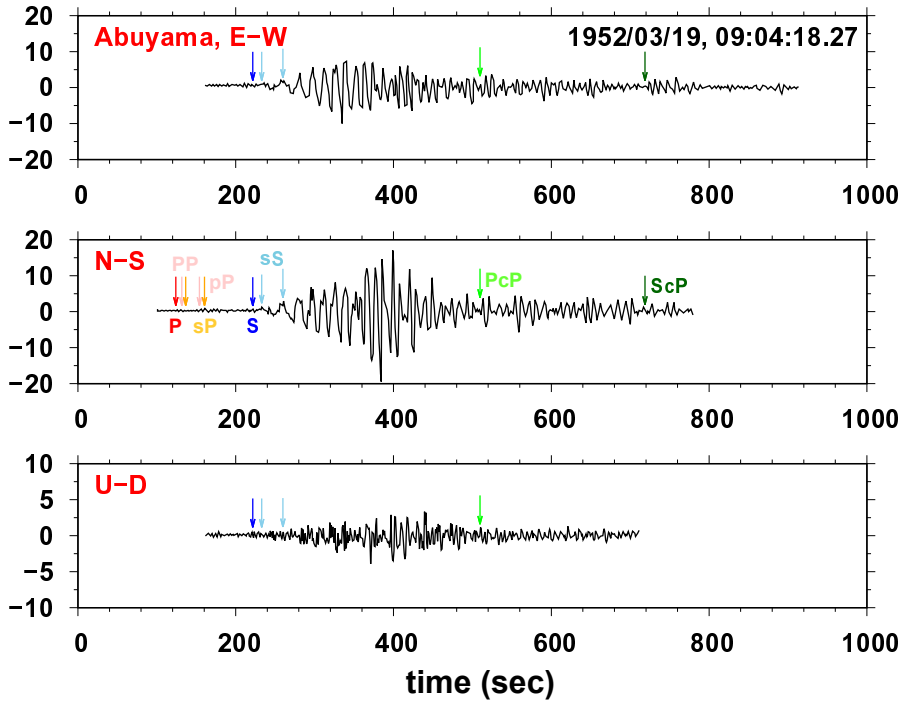


**Figure S1.** Three-component raw seismic record sections at station in Abuyama. Lapse time after 09:04:18.27 in March 19, 1952 (UTC) is presented. Theoretical arrival times of major phases are marked.

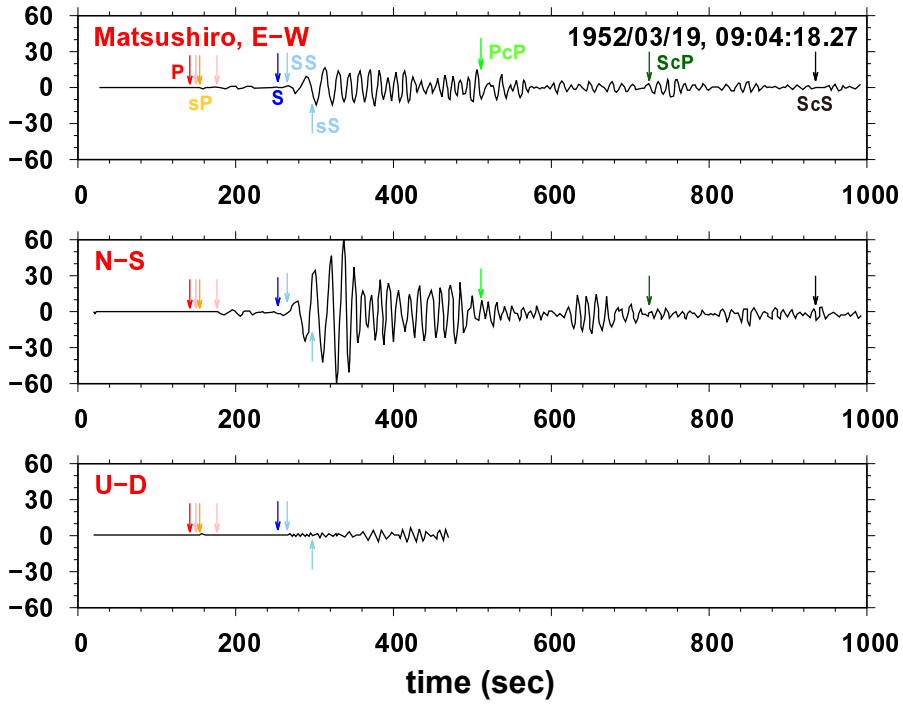


**Figure S2.** Three-component raw seismic record sections at station in Matsushiro. Lapse time after 09:04:18.27 in March 19, 1952 (UTC) is presented. Theoretical arrival times of major phases are marked.

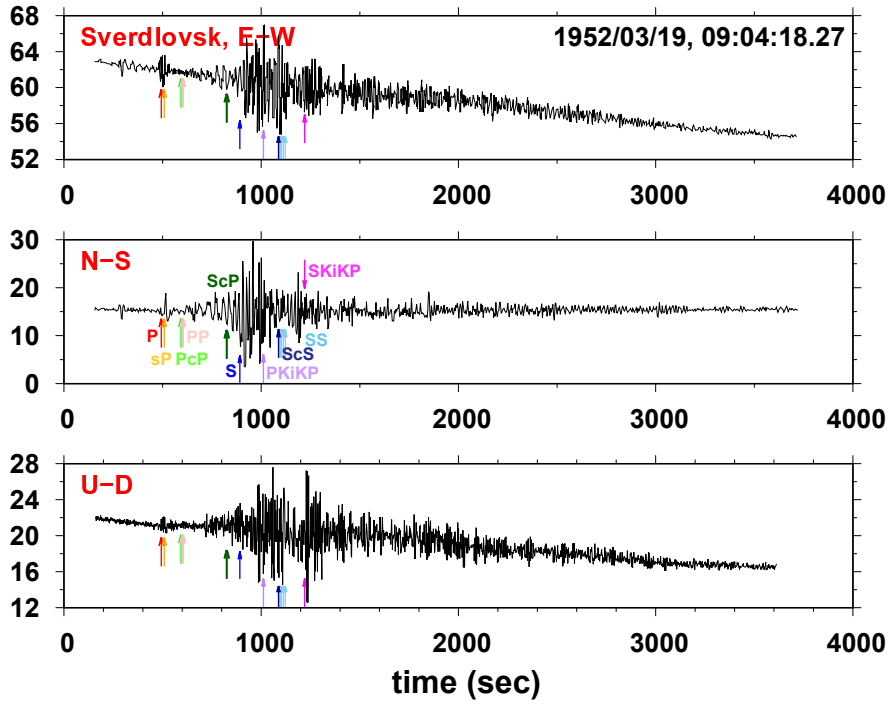


**Figure S3.** Three-component raw seismic record sections at station in Sverdlovsk. Lapse time after 09:04:18.27 in March 19, 1952 (UTC) is presented. Theoretical arrival times of major phases are marked. The inclined record sections are corrected before waveform analysis.

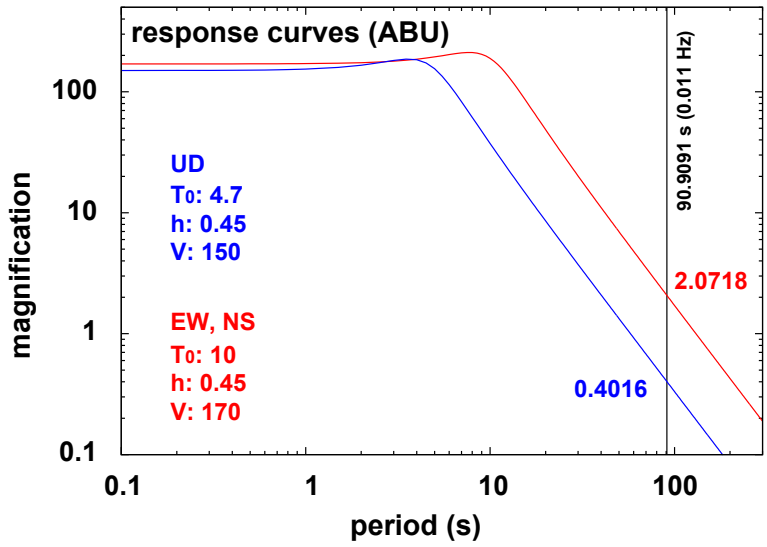


**Figure S4.** Instrument response functions of vertical (UD) and horizontal (EW, NS) components of station ABU. The amplification at 0.011 Hz is indicated.

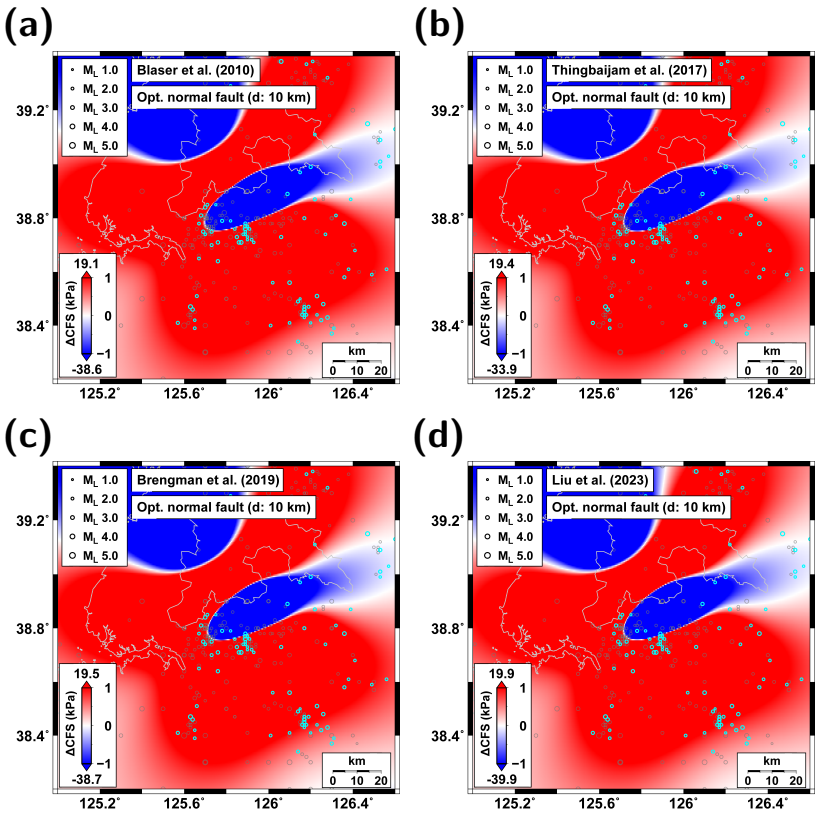


**Figure S5.** Coulomb stress changes induced by the 19 March 1952 $M_W$ 6.3 suburban Pyongyang earthquake for optimally oriented normal faults at a depth of 10 km based on empirical source-parameter relationships of (a) Blaser et al. (2010), (b) Thingbaijam et al. (2017), (c) Brengman et al. (2019), and (d) Liu et al. (2023). The observed induced stress fields are similar among the different relationships.

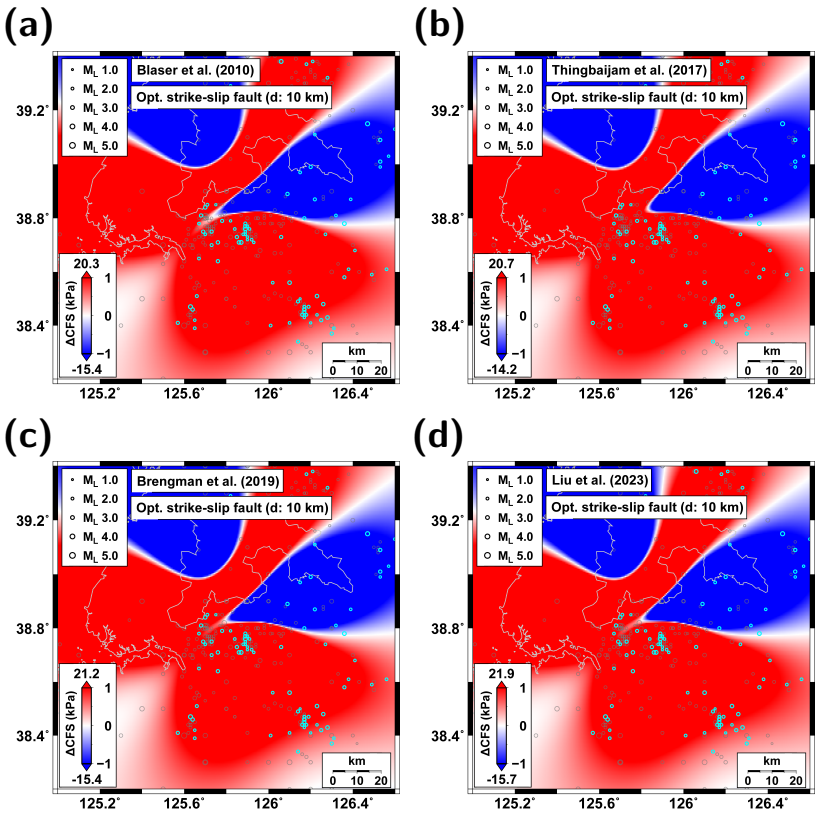


**Figure S6.** Coulomb stress changes induced by the 19 March 1952 $M_W$ 6.3 suburban Pyongyang earthquake for optimally oriented strike-slip faults at a depth of 10 km based on empirical source-parameter relationships of (a) Blaser et al. (2010), (b) Thingbaijam et al. (2017), (c) Brengman et al. (2019), and (d) Liu et al. (2023). The observed induced stress fields are similar among the different relationships.

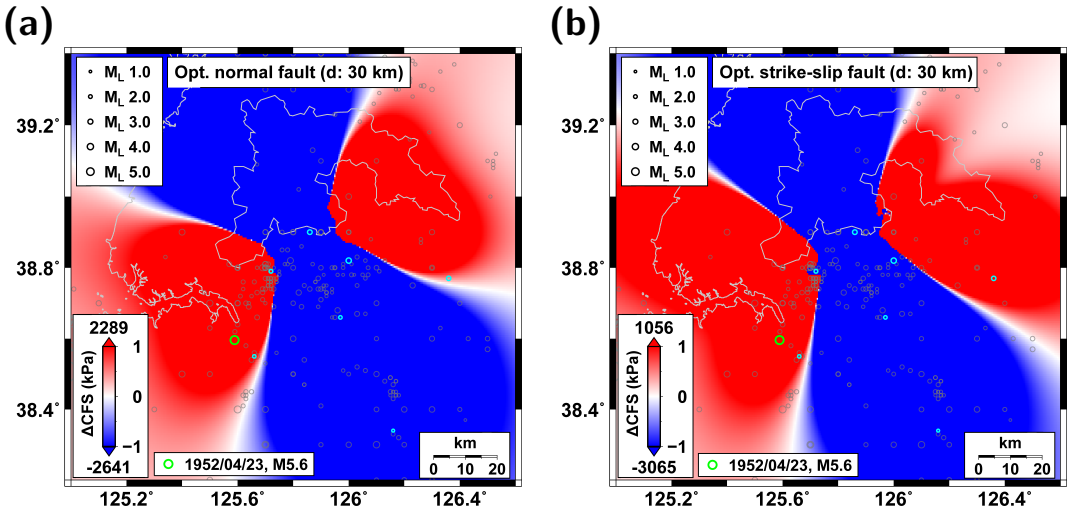


**Figure S7.** Coulomb stress changes induced by the 19 March 1952 $M_W$ 6.3 suburban Pyongyang earthquake for (a) optimally oriented normal faults and (b) optimally oriented strike-slip faults at a depth of 30 km. Seismicity from 1978-2024 is marked. The focal depths of events are less than 20 km (circles). The northern and southern regions present stress decrease, suggesting low possibility of event induction.

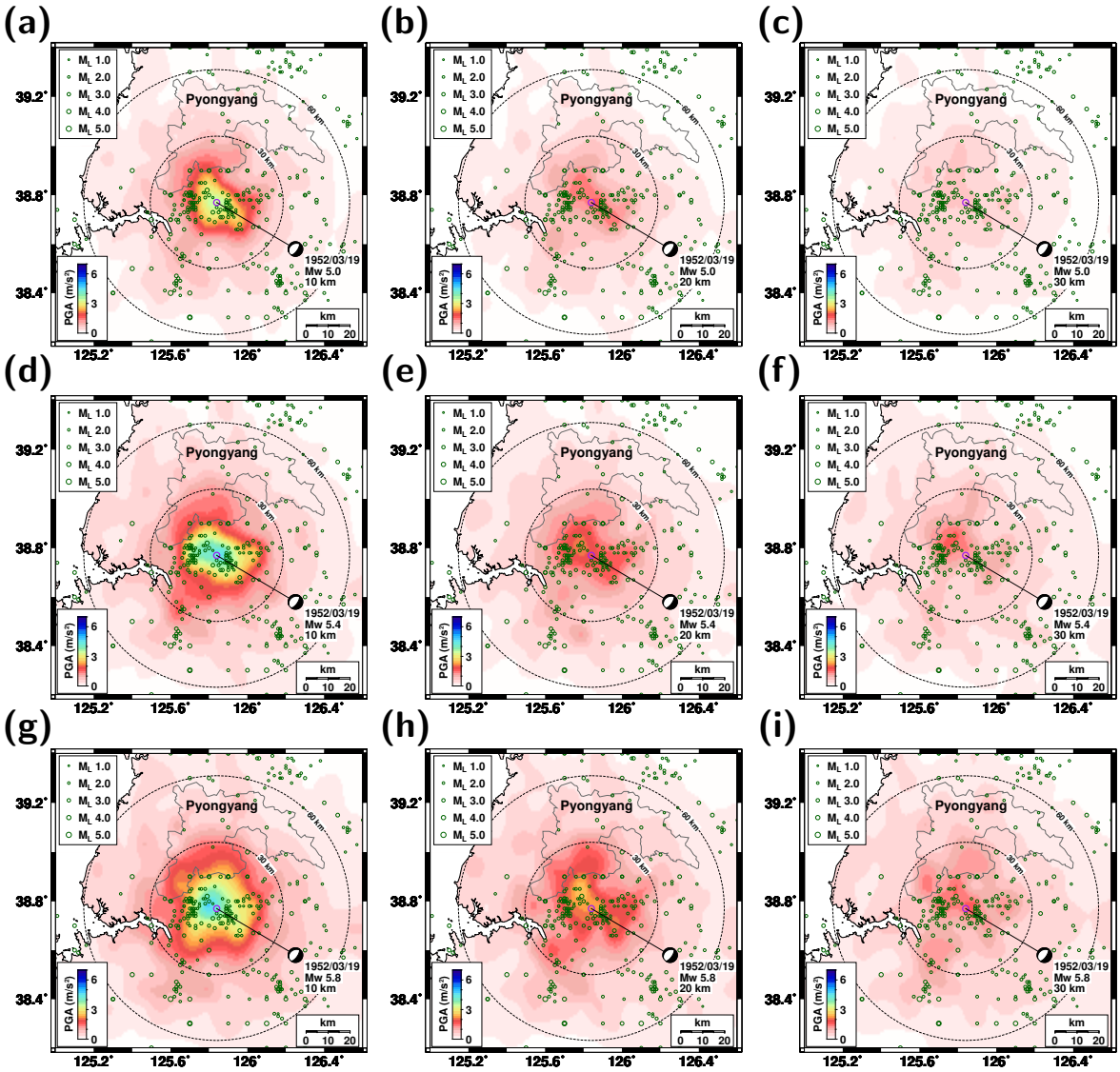


**Figure S8.** Numerical simulation of peak ground accelerations (PGAs) for earthquakes with magnitudes $M_W$ 5.0 at focal depths of (a) 10 km, (b) 20 km, and (c) 30 km, $M_W$ 5.4 at focal depths of (d) 10 km, (e) 20 km, and (f) 30 km, and $M_W$ 5.8 at focal depths of (g) 10 km, (h) 20 km, and (i) 30 km. The seismicity in the region is presented (circles).

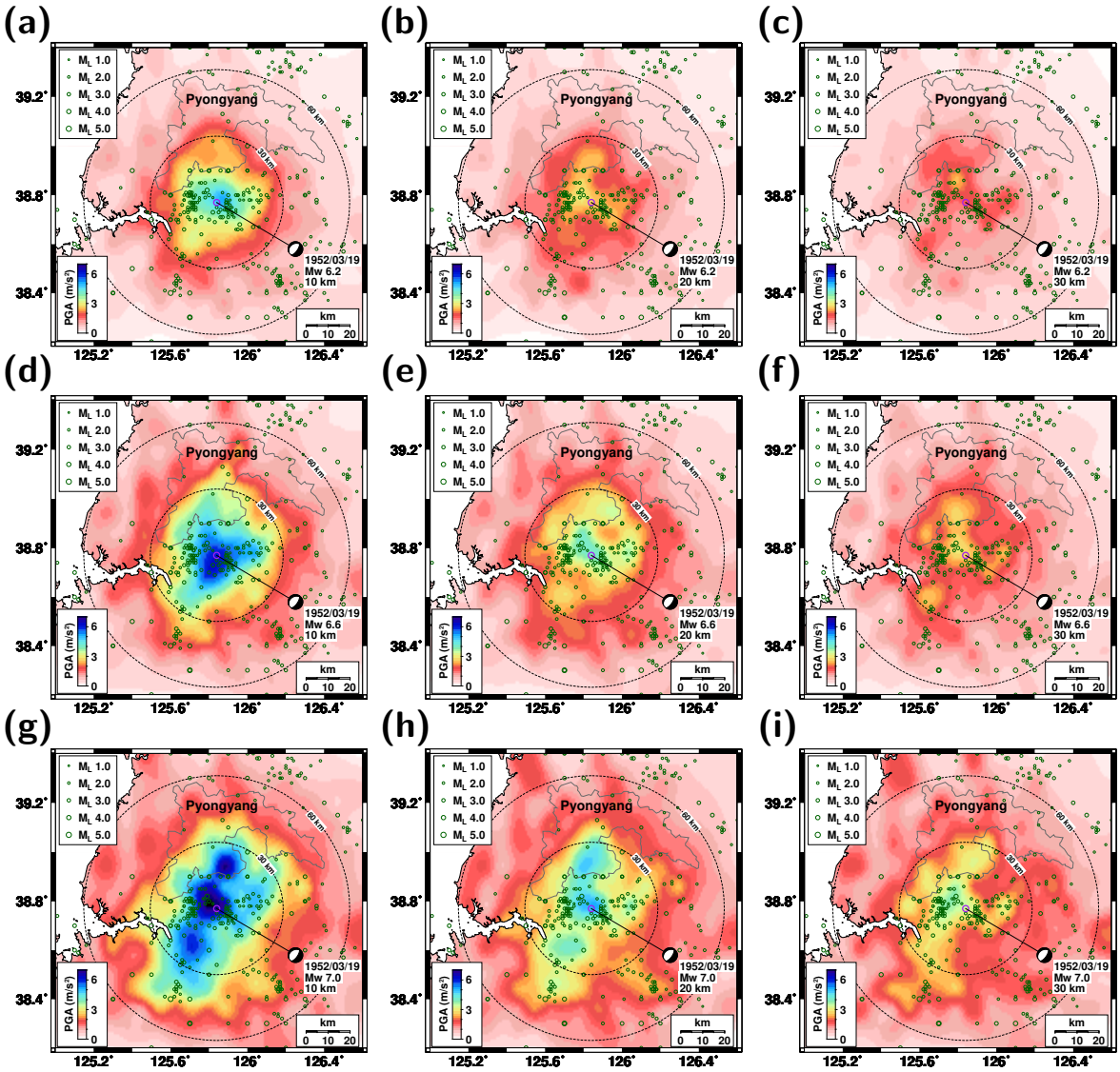


**Figure S9.** Numerical simulation of peak ground accelerations (PGAs) for earthquakes with magnitudes $M_W$ 6.2 at focal depths of (a) 10 km, (b) 20 km, and (c) 30 km, $M_W$ 6.6 at focal depths of (d) 10 km, (e) 20 km, and (f) 30 km, and $M_W$ 7.0 at focal depths of (g) 10 km, (h) 20 km, and (i) 30 km. The seismicity in the region is presented (circles).

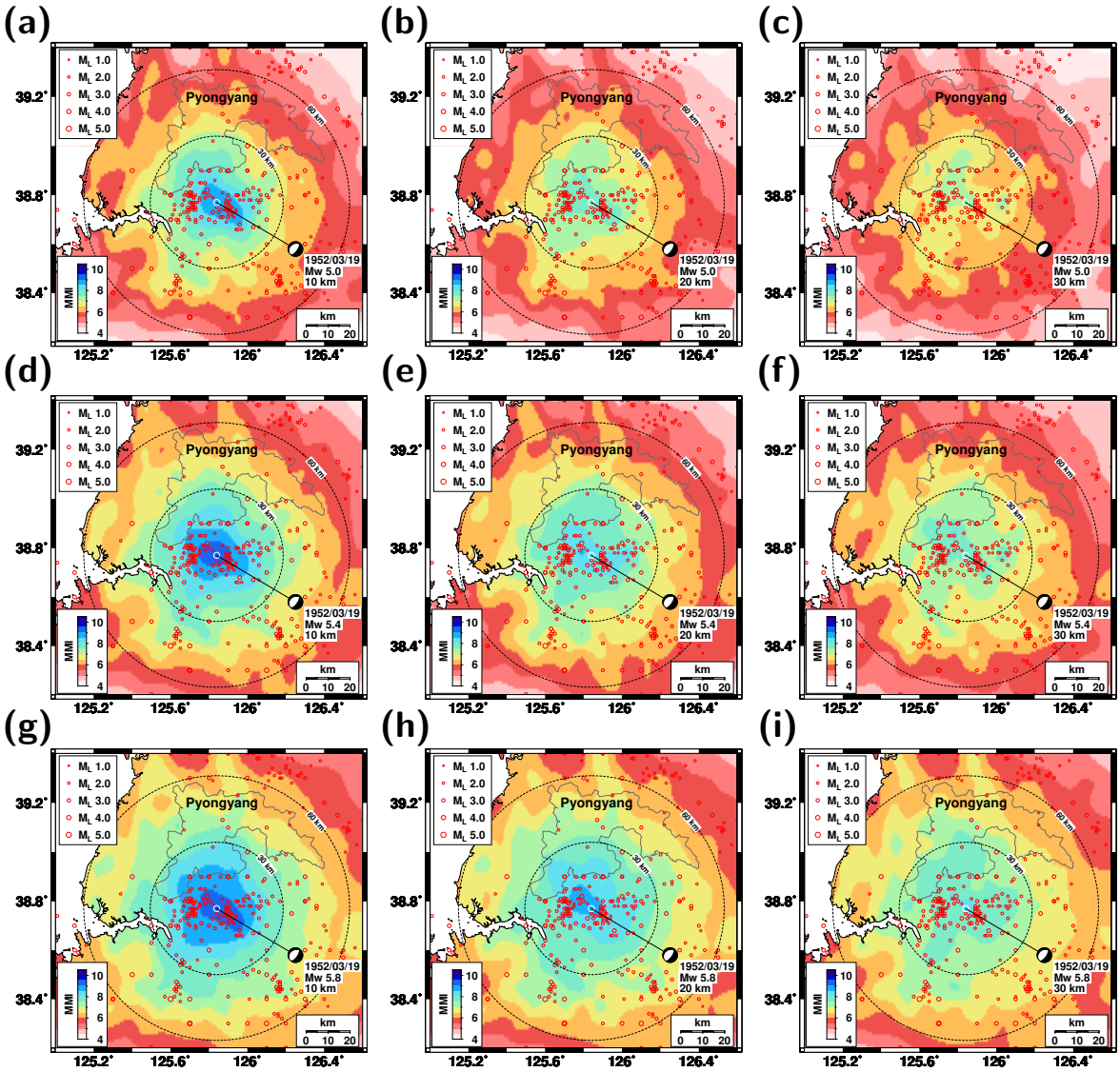


**Figure S10.** Numerical simulation of seismic intensities for earthquakes with magnitudes $M_W$ 5.0 at focal depths of (a) 10 km, (b) 20 km, and (c) 30 km, $M_W$ 5.4 at focal depths of (d) 10 km, (e) 20 km, and (f) 30 km, and $M_W$ 5.8 at focal depths of (g) 10 km, (h) 20 km, and (i) 30 km. The seismicity in the region is presented (circles).

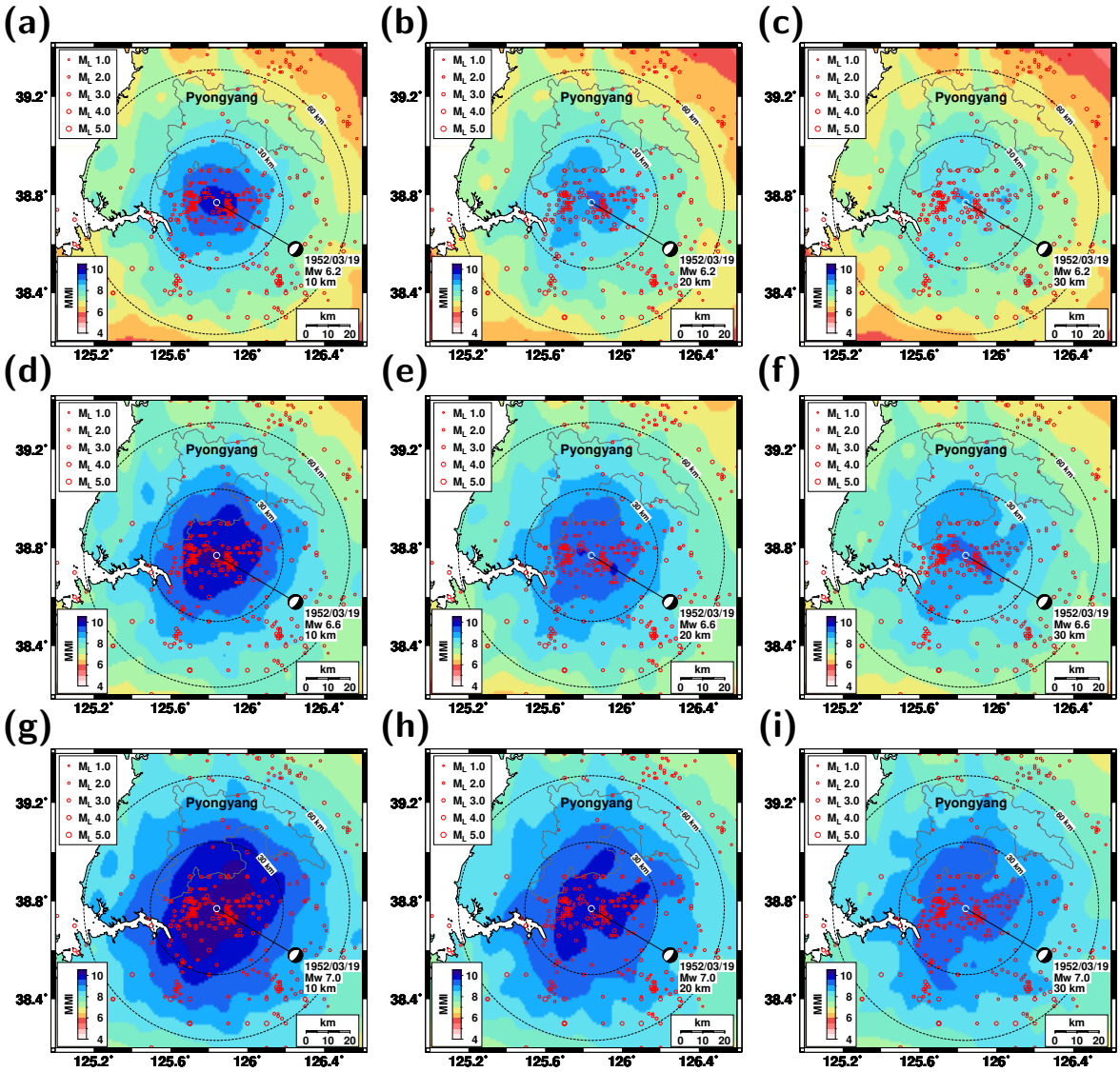


**Figure S11.** Numerical simulation of seismic intensities for earthquakes with magnitudes $M_W$ 6.2 at focal depths of (a) 10 km, (b) 20 km, and (c) 30 km, $M_W$ 6.6 at focal depths of (d) 10 km, (e) 20 km, and (f) 30 km, and $M_W$ 7.0 at focal depths of (g) 10 km, (h) 20 km, and (i) 30 km. The seismicity in the region is presented (circles).